

# Hydrogenated Cs<sub>2</sub>AgBiBr<sub>6</sub> for High-Efficient Lead-Free Inorganic Double Perovskite Solar Cell

Zeyu Zhang

Beijing University of Technology

Qingde Sun

Beijing Computational Science Research Center

Yue Lu

Beijing University of Technology

Feng Lu

Nankai University

Xulin Mu

Beijing University of Technology

Su-Huai Wei

Beijing Computational Science Research Center <https://orcid.org/0000-0003-1563-4738>

Manling Sui (✉ [mlsui@bjut.edu.cn](mailto:mlsui@bjut.edu.cn))

Beijing University of Technology <https://orcid.org/0000-0002-0415-5881>

---

## Article

**Keywords:** hydrogenated Cs<sub>2</sub>AgBiBr<sub>6</sub>, perovskite, inorganic PSCs

**Posted Date:** June 15th, 2021

**DOI:** <https://doi.org/10.21203/rs.3.rs-587497/v1>

**License:** © ⓘ This work is licensed under a Creative Commons Attribution 4.0 International License.

[Read Full License](#)

---

**Version of Record:** A version of this preprint was published at Nature Communications on June 13th, 2022. See the published version at <https://doi.org/10.1038/s41467-022-31016-w>.

# Hydrogenated $\text{Cs}_2\text{AgBiBr}_6$ for High-Efficient Lead-Free Inorganic Double Perovskite Solar Cell

Zeyu Zhang<sup>1</sup>, Qingde Sun<sup>2</sup>, Yue Lu<sup>1\*</sup>, Feng Lu<sup>3</sup>, Xulin Mu<sup>1</sup>, Su-Huai Wei<sup>2\*</sup>, Manling Sui<sup>1\*</sup>

<sup>1</sup>Beijing Key Laboratory of Microstructure and Properties of Solids, Faculty of Materials and Manufacturing, Beijing University of Technology, Beijing, 100124, China

<sup>2</sup>Beijing Computational Science Research Center, Beijing 100193, China

<sup>3</sup>Department of Electronic Science and Engineering, and Tianjin Key Laboratory of Photo-Electronic Thin Film Device and Technology, Nankai University, Tianjin 300071, China

Corresponding author: [luyue@bjut.edu.cn](mailto:luyue@bjut.edu.cn), [suhuaiwei@csrc.ac.cn](mailto:suhuaiwei@csrc.ac.cn), [mlsui@bjut.edu.cn](mailto:mlsui@bjut.edu.cn)

**Development of the stable, lead-free inorganic perovskite material is of greatly importance on fabricating the third-generation solar cell. Until now, double perovskite, such as  $\text{Cs}_2\text{AgBiBr}_6$ , has been proved to be one of the most potential candidates to solve the toxicity and stability issues of traditional lead halide perovskite solar cells (PSCs). However, due to a wide and indirect bandgap of  $\text{Cs}_2\text{AgBiBr}_6$  film, its light absorption ability is largely limited and the photoelectronic conversion efficiency (PCE) is normally lower than 2.5%. In this text, by using a hydrogenation method, the bandgap ( $E_g$ ) of  $\text{Cs}_2\text{AgBiBr}_6$  films could be tunable from 2.14 eV to 1.61 eV. At the same time, the highest PCE of hydrogenated  $\text{Cs}_2\text{AgBiBr}_6$  perovskite solar cell has been improved more than 150% up to 6.27%. To the**

**best of our knowledge, this is a record high efficiency of  $\text{Cs}_2\text{AgBiBr}_6$ -based perovskite solar cell. Further investigations confirmed that the interstitial doping of atomic hydrogen ( $\text{H}^*$ ) in  $\text{Cs}_2\text{AgBiBr}_6$  lattice could not only adjust its valence and conduction band energy levels, but also optimize the carrier mobility from  $1.71 \text{ cm}^2\text{V}^{-1}\text{s}^{-1}$  to  $9.28 \text{ cm}^2\text{V}^{-1}\text{s}^{-1}$  and enhance the carrier lifetime from 18.85 ns to 41.86 ns. All these works provide a new strategy to fabricate the high performance lead-free inorganic PSCs.**

## **Introduction**

As one of the significant developments of third-generation solar cells, organic-inorganic halide perovskites (OIHP) have attracted tremendous attentions since their highest photoelectronic conversion efficiency (PCE) is now approaching 25.5%<sup>1</sup>, comparable to the silicon-based solar cells. Traditionally, the OIHP materials have a stoichiometric ratio of  $\text{ABX}_3$ , in which the A, B and X sites are consisted of organic cation (Methylamine cation ( $\text{MA}^+$ ) or Formamidine cation ( $\text{FA}^+$ )), metal cation  $\text{Pb}^{2+}$  and halide anions ( $\text{Cl}^-$ ,  $\text{Br}^-$  and  $\text{I}^-$ ), respectively<sup>2-5</sup>. Despite the excellent photovoltaic performance of OIHP solar cells, there still exist two critical issues that hinder their widely applications in industry<sup>6-8</sup>. The first aspect is the intrinsic instability of the OIHP caused by the volatility of organic components, and the other is the disreputable toxicity of lead element. To solve these problems, extensive efforts have been done to explore the Pb-free inorganic perovskite materials as the core adsorbent layer in solar cell<sup>9-13</sup>. For example, it has been reported that the substitution of  $\text{MA}^+$  with  $\text{Cs}^+$  cations in A site could increase the decomposition energy of perovskite from -0.111 eV ( $\text{MAPbI}_3$ ) to -0.069 eV ( $\text{CsPbI}_3$ )<sup>14</sup>, thereby enhancing the stability. Considering on the toxicity of Pb element in B site of perovskite, tin cation ( $\text{Sn}^{2+}$ ) or silver cation

( $\text{Ag}^+$ ) combined with bismuth cation ( $\text{Bi}^{3+}$ ) are alternative substitutions to relieve the toxicity of the optical absorption layer. Nevertheless, the susceptible  $\text{Sn}^{2+}$  is easily oxidized to  $\text{Sn}^{4+}$  in air, which rapidly decreases the photovoltage performance of  $\text{CsSnI}_3$ -based solar cells<sup>15,16</sup>. While, the double substitutions of  $\text{Pb}^{2+}$  utilizing B-site cations such as  $\text{Ag}^+$  and  $\text{Bi}^{3+}$  in perovskite could effectively improve the stability due to its enhanced Coulomb interaction energy, which leads to a high positive decomposition energy in  $\text{Cs}_2\text{AgBiBr}_6$  (0.38 eV)<sup>17</sup>. Thus,  $\text{Cs}_2\text{AgBiBr}_6$ -based perovskite solar cell (PSC) is one of the most promising candidates in inorganic lead-free perovskite photovoltaic devices.

However, until now, the champion PCE of  $\text{Cs}_2\text{AgBiBr}_6$  PSC was just 2.5%<sup>18</sup>, which is much lower than that of organic-inorganic hybrid lead-based PSCs. Therefore, the improvement of PCE in  $\text{Cs}_2\text{AgBiBr}_6$  PSC is urgently needed. There are three main factors restricting the improvement of the efficiency, including the large bandgap ( $E_g$ ), low carrier mobility and carrier lifetime. The  $\text{Cs}_2\text{AgBiBr}_6$  has an indirect measured bandgap of 1.83 eV-2.19 eV<sup>19,20</sup>, which limits the light absorption of low energy photons in the perovskite layer. Meanwhile, the carrier mobility of  $\text{Cs}_2\text{AgBiBr}_6$  is only about  $1.00 \text{ cm}^2\text{V}^{-1}\text{s}^{-1}$ - $11.81 \text{ cm}^2\text{V}^{-1}\text{s}^{-1}$ , which is quite smaller than the one in  $\text{MAPbI}_3$  (about  $35 \text{ cm}^2\text{V}^{-1}\text{s}^{-1}$ )<sup>21-23</sup>. In addition, the carrier lifetime of thin-film  $\text{Cs}_2\text{AgBiBr}_6$  is only about 13.7 ns due to a large number of defect states at the grain boundaries of the films<sup>24,25</sup>.

In order to improve the PCE of  $\text{Cs}_2\text{AgBiBr}_6$  PSC, extensive efforts have been tried to improve the carrier transport properties. For example, Wang et al. successfully developed a vapor-deposition method to fabricate the  $\text{Cs}_2\text{AgBiBr}_6$  perovskite film with dense grains, whose defect density

( $2.13 \times 10^{16} \text{ cm}^{-3}$ )<sup>26</sup> was lower than that of the solution method ( $9.1 \times 10^{16} \text{ cm}^{-3}$ )<sup>27</sup>. Gao et al. spin-coated an excellent  $\text{Cs}_2\text{AgBiBr}_6$  film with the grain size of 410 nm via a proper anti-solvent technology, the defect density of perovskite film has been decreased significantly and the PCE of  $\text{Cs}_2\text{AgBiBr}_6$  perovskite solar cells has been improved up to 2.2%<sup>28</sup>. On the other side, reducing the bandgap  $E_g$  of  $\text{Cs}_2\text{AgBiBr}_6$  perovskite has been achieved in single crystals. For example, Li et al. successfully decreased the  $E_g$  value of single crystal  $\text{Cs}_2\text{AgBiBr}_6$  from 2.19 eV to 1.7 eV by applied a high pressure of 15 GPa, however, the crystal structure as well as the  $E_g$  value recovered rapidly as the pressure is removed<sup>29</sup>. Recently, by adjusting the degree of Ag-Bi disorder, Ji et al. achieved the decrease of bandgap from 1.98 eV to 1.72 eV in single crystal  $\text{Cs}_2\text{AgBiBr}_6$ , which was grown at high evaporation temperature of 150 °C<sup>30</sup>. This result is consistent with the predication of Yang et al. based on density functional theory (DFT) calculations that the bandgap of  $\text{Cs}_2\text{AgBiBr}_6$  could be effectively decreased from 1.93 eV to 0.44 eV after disordering at the (Ag, Bi) sublattice<sup>31</sup>. However, due to unsuitable pressure and temperature preparation conditions, such effective crystal-engineering approaches for the reduction of bandgap could not be implemented in the spin-coated  $\text{Cs}_2\text{AgBiBr}_6$  thin films for the fabrication of PSC devices. Therefore, the critical issue is the feasibility of the strategy of reducing bandgap in the perovskite thin films and its realizability in perovskite solar cells. In this text, by using a hydrogenation method, atomic hydrogen could be successfully doped into the interstitial sites of  $\text{Cs}_2\text{AgBiBr}_6$  crystal lattice, which modified the bandgap of high-quality double perovskite  $\text{Cs}_2\text{AgBiBr}_6$  films from 2.14 eV to 1.61 eV. Based on this, the highest PCE of hydrogenated  $\text{Cs}_2\text{AgBiBr}_6$ -based PSC has been improved for more than 150% up to 6.27%, which is the record-high efficiency so far. Moreover, the hydrogenated  $\text{Cs}_2\text{AgBiBr}_6$  films exhibit extraordinary stability under light illumination or at

temperature of 85 °C in nitrogen environment.

As shown in [Fig. 1a](#), high quality  $\text{Cs}_2\text{AgBiBr}_6$  films were firstly fabricated by using a traditional one-step spin-coating solution method (details see Method), which have a face-centered cubic structure phase ( $\text{Fm}\bar{3}\text{m}$ ) (the black spectrum in [Fig. 1b](#)) and present a yellow color (the optical image of the pristine sample insets in [Fig. 1b](#)). Then the perovskite films were hydrogenated for different times (600 s and 1,200 s) by using plasma treatment in a hydrogen ( $\text{H}_2$ ) and argon ( $\text{Ar}$ ) mixed gas environment ([Fig. 1a](#), see Method). When the hydrogenation time is up to 1,200 s, the  $\text{Cs}_2\text{AgBiBr}_6$  perovskite films remain to be the cubic phase ( $\text{Fm}\bar{3}\text{m}$ ) without any phase transition ([Fig. 1b](#)), but the color of the films change from yellow into black (insert pictures in [Fig. 1b](#)) and the surface morphology of perovskite film becomes smoother ([Fig. 1c](#)). However, when the hydrogenation time exceeds 1,800 s, additional XRD peak at  $29.5^\circ$  begins to appear, which corresponds to the  $\text{CsBr}$  phase (110) and indicates the damage of host (standard)  $\text{Cs}_2\text{AgBiBr}_6$  lattice after an excessive hydrogenation treatment ([Supplementary Fig. 1](#)).

To quantitatively analyze the color change of the hydrogenated  $\text{Cs}_2\text{AgBiBr}_6$  films, optical absorption of these perovskite films was investigated by Ultraviolet-visible absorption spectra (UV-vis) as shown in [Fig. 1d](#). When increasing the hydrogenation time from 0 s to 1,200 s, the light absorption for photons with wavelength above 483 nm exhibits an obvious increase, which indicates an effective improvement of visible light absorption of the hydrogenated  $\text{Cs}_2\text{AgBiBr}_6$  perovskite films. Meanwhile, the bandgap of hydrogenated  $\text{Cs}_2\text{AgBiBr}_6$  films is also consistent with the measured one determined by the tauc plots equation,

$$(\alpha h\nu)^{1/n} = A(h\nu - E_g) \quad (1)$$

where  $\alpha$  is absorption coefficient,  $h$  is Plank's constant,  $\nu$  is the incident frequency,  $A$  is a constant of proportionality<sup>32</sup> and the exponent  $n$  is 2 for indirect bandgap semiconductor<sup>33</sup>. As shown in Fig. 1e and Supplementary Fig. 2, the pristine Cs<sub>2</sub>AgBiBr<sub>6</sub> film is an indirect semiconductor with a bandgap value of 2.14 eV, which is consistent with previous reports<sup>19,20</sup>. However, after hydrogenating the Cs<sub>2</sub>AgBiBr<sub>6</sub> films for 600 s and 1,200 s, the treated Cs<sub>2</sub>AgBiBr<sub>6</sub> films are still indirect semiconductors, and their bandgap values have been decreased from 2.14 eV to 1.86 eV and further to 1.61 eV, respectively (Fig. 1e).

In addition to the bandgap value, the carrier mobility, carrier concentration and carrier lifetime are critically important for the performance of perovskite solar cells. The carrier mobility in the pristine Cs<sub>2</sub>AgBiBr<sub>6</sub> film was about 1.71 cm<sup>2</sup>V<sup>-1</sup>s<sup>-1</sup> and obtained from the Hall effect measurement data (Supplementary Fig. 3). After hydrogenating the Cs<sub>2</sub>AgBiBr<sub>6</sub> film for 600 s, the carrier mobility (3.17 cm<sup>2</sup>V<sup>-1</sup>s<sup>-1</sup>) increases by 85%. As elongating the hydrogenation time to 1,200 s, the carrier mobility (9.28 cm<sup>2</sup>V<sup>-1</sup>s<sup>-1</sup>) increases up to 542%, as compared with the one in the pristine Cs<sub>2</sub>AgBiBr<sub>6</sub> film (Fig. 1f). Meanwhile, the carrier concentration of Cs<sub>2</sub>AgBiBr<sub>6</sub> film has been improved from  $1.42 \times 10^{12}$  cm<sup>-3</sup> to  $2.51 \times 10^{12}$  cm<sup>-3</sup> and further to  $5.96 \times 10^{12}$  cm<sup>-3</sup> after 600 s and 1,200 s hydrogenation treatment (Fig. 1f), which is mostly ascribing to the enhancement of light absorption range above 483 nm. Finally, an obvious increase of the carrier lifetime from 18.85 ns to 30.67 ns and further to 41.86 ns in hydrogenated Cs<sub>2</sub>AgBiBr<sub>6</sub> film has been detected (inset in Fig. 1g, Supplementary Fig. 4 and Supplementary Table 1) after hydrogenation treatment of the Cs<sub>2</sub>AgBiBr<sub>6</sub> films for 600 s and 1,200 s, respectively.

In order to explore the influence of H\* on Cs<sub>2</sub>AgBiBr<sub>6</sub>, the distribution of H\* in Cs<sub>2</sub>AgBiBr<sub>6</sub> film needs to be studied. After hydrogenating the perovskite films from 0 s-3,000 s, the color evolution rate of the front (surface exposed in the hydrogen plasma environment) and back (see from the glass side of the film) sides of the Cs<sub>2</sub>AgBiBr<sub>6</sub> films is quite different ([Fig. 2a](#)). In order to quantify the variation tendency for the front and back sides of the hydrogenated Cs<sub>2</sub>AgBiBr<sub>6</sub> films, the blackness of the optical images on both sides was counted up as a change of hydrogenation time (black and red curves in [Fig. 2a](#)). It is clearly identified that the blackness keeps increasing gradually with the hydrogenation time increase, and the blackness of front side is always higher than the one of back side, especially when hydrogenating the Cs<sub>2</sub>AgBiBr<sub>6</sub> film for 600 s-1,800 s. After 1,800 s hydrogenation treatment, the blackness difference of front and back sides becomes smaller. All these results indicate that the H\* concentration in the hydrogenated Cs<sub>2</sub>AgBiBr<sub>6</sub> film has a gradient distribution depending on the positng and hydrogenating time.

During the hydrogenation treatment of Cs<sub>2</sub>AgBiBr<sub>6</sub> film (Method), H\* needs to diffuse firstly from the front side into the inner of perovskite film, so it obviously obeys the constant surface concentration diffusion mode<sup>34</sup>

$$\frac{C}{C_s} = erfc \left( \frac{x}{2\sqrt{Dt}} \right) \quad (2)$$

where  $x$  is the diffusion thickness,  $D$  is diffusion coefficient of H\* in Cs<sub>2</sub>AgBiBr<sub>6</sub> film,  $t$  is the hydrogenation time,  $C_s$  is diffusion source concentration ( $x=0$ ) and  $C$  is concentration at the depth  $x$  in film. However, due to the uncertainty of the diffusion coefficient of H\* in Cs<sub>2</sub>AgBiBr<sub>6</sub>, it is hard to predict quantitatively the H\* distribution concentration in perovskite film. The diffusion coefficient of H\* in most materials ranges from  $4.9 \times 10^{-15}$  cm<sup>2</sup>/s to  $1.07 \times 10^{-5}$  cm<sup>2</sup>/s ([Supplementary](#)

**Table 2)**<sup>35-42</sup>. So here, to estimate the diffusion coefficient, we first simulated the depth-dependent  $\frac{C}{C_s}$  values at different hydrogenation times (600 s, 1,200 s, 1,800 s, 2,400 s and 3,000 s) based on the selected diffusion coefficients from  $1 \times 10^{-15} \text{ cm}^2/\text{s}$  to  $1 \times 10^{-5} \text{ cm}^2/\text{s}$ , as shown in [Supplementary Figs. 5a-5e, respectively](#). At a maximum film thickness of 140 nm ([Supplementary Fig. 5f](#)), the simulated  $\frac{C}{C_s}$  values are shown in [Supplementary Fig. 5](#) and summarized in [Supplementary Table 3](#). Considering the simulated  $\frac{C}{C_s}$  value at the real film thickness should be comparable to the image blackness (details see Method and [Fig. 2a](#)) ratio at the front and back sides of hydrogenated  $\text{Cs}_2\text{AgBiBr}_6$  film ([Supplementary Fig. 5g](#) and [Supplementary Table 3](#)), the real diffusion coefficient  $D$  of  $\text{H}^*$  in  $\text{Cs}_2\text{AgBiBr}_6$  is then estimated to range from about  $1 \times 10^{-14} \text{ cm}^2/\text{s}$  to  $1 \times 10^{-13} \text{ cm}^2/\text{s}$ . [Figure 2b](#) shows a schematic diagram of  $\text{H}^*$  diffusion in the hydrogenated  $\text{Cs}_2\text{AgBiBr}_6$  film of 1,200 s.

After the diffusion of  $\text{H}^*$  into the  $\text{Cs}_2\text{AgBiBr}_6$  lattice, the perovskite films exhibit extraordinary stability undergoing long-term high temperature (85 °C) or 1 sun light illuminating treatments ([Fig. 2c](#) and [Fig. 2d](#)). After 80 day ageing process, these hydrogenated  $\text{Cs}_2\text{AgBiBr}_6$  films keep optically black, indicating their superior stability in  $\text{N}_2$  environment with light and heat treatments. The excellent photoelectric properties of hydrogenated perovskite films mentioned above ([Fig. 1](#)) suggest that the hydrogenated  $\text{Cs}_2\text{AgBiBr}_6$  should have great application potential in the lead-free perovskite solar cell. In order to fabricate the perovskite solar cell practically, energy level of hydrogenated  $\text{Cs}_2\text{AgBiBr}_6$  needs to be firstly determined as shown in [Fig. 2e](#). Here, the ultraviolet photoelectron spectroscopy (UPS) characterizations confirm that the work function  $\phi$  of 0 s, 600 s and 1,200 s hydrogenated  $\text{Cs}_2\text{AgBiBr}_6$  films were -5.27 eV, -4.39 eV and -3.89 eV, and the energy

gap  $\Delta E$  between the  $E_{VBM}$  and Fermi level were 0.93 eV, 1.26 eV and 1.44 eV ([Supplementary Fig. 6](#)), respectively. Combining with the bandgap values in [Fig. 1e](#), the energy level of maximum valence band ( $E_{VBM}$ ) and minimum conduction band ( $E_{CBM}$ ) of hydrogenated  $\text{Cs}_2\text{AgBiBr}_6$  films could be obtained as shown in [Fig. 2e](#) (details see [Supplementary Fig. 6](#)).

To make sure the compatibility of energy level in PSC, we selected  $\text{SnO}_2$ , Spiro-OMeTAD, ITO and Au as the electron transport layer (ETL), hole transport layer (HTL) and electrodes ([Fig. 2f](#)), respectively. And the PSC device was successfully prepared as shown in [Fig. 3a](#), in which the layer structures could be identified clearly. In order to explore the effect of hydrogenation treatment on the microstructure of  $\text{Cs}_2\text{AgBiBr}_6$  film, we took the HAADF images from the surface portions of the pristine and hydrogenated  $\text{Cs}_2\text{AgBiBr}_6$  films as shown in [Fig. 3b](#). It is obvious that the pristine film presents perfect atomic arrangement of cubic  $\text{Cs}_2\text{AgBiBr}_6$  phase. However, after 1,200 s hydrogenation, the angle between  $(0\bar{4}0)$  and  $(004)$  lattice planes (projection from [100] zone axis) was  $86.8^\circ$ , which is smaller than the standard  $90^\circ$ , indicating the insertion of  $\text{H}^*$  could induce a slight lattice distortion on the surface of hydrogenated  $\text{Cs}_2\text{AgBiBr}_6$  film.

More importantly, the pristine  $\text{Cs}_2\text{AgBiBr}_6$ -based PSC exhibits a low PCE of only about 0.55%, and the short-circuit current density ( $J_{sc}$ ) is  $1.03 \text{ mA cm}^{-2}$  (see black lines and dots in [Figs. 3c](#) and [3d](#)). After hydrogenating the  $\text{Cs}_2\text{AgBiBr}_6$  films for 600 s and 1,200 s, although the open-circuit voltage ( $V_{oc}$ ) has a little increase from 0.88 V to 0.91 V, the short-circuit current density ( $J_{sc}$ ) increases significantly from  $1.03 \text{ mA cm}^{-2}$  to  $7.04 \text{ mA cm}^{-2}$  and further to  $8.86 \text{ mA cm}^{-2}$  ([Fig. 3c](#)). Meanwhile, the average PCE of hydrogenated  $\text{Cs}_2\text{AgBiBr}_6$  is effectively improved from 0.42% (0

s) to 2.93% (600 s) and then to 5.56% (1,200 s) ([Fig. 3d](#)). Finally, the highest PCE in the 1,200 s hydrogenated  $\text{Cs}_2\text{AgBiBr}_6$  PSC devices presents a maximum PCE value of 6.27% (blue in [Fig. 3d](#)). And this is the record high efficiency in the  $\text{Cs}_2\text{AgBiBr}_6$ -based PSC devices so far. Meanwhile, the average short-circuit current density ( $J_{sc}$ ) increases from  $0.92 \text{ mA cm}^{-2}$  to  $6.29 \text{ mA cm}^{-2}$  and then to  $10.13 \text{ mA cm}^{-2}$  ([Fig. 3e](#)), the average open-circuit voltage ( $V_{oc}$ ) increases from 0.83 V to 0.84 V and then to 0.87 V ([Fig. 3f](#)) and the FF increases from 54.95% to 56.17% and then to 63.84% ([Fig. 3g](#)), respectively. All the statistical analysis (at least 50 devices) exhibited the best PSC performance was present on the 1,200 s hydrogenated  $\text{Cs}_2\text{AgBiBr}_6$  PSC.

In order to explore the effect of  $\text{H}^*$  on the efficiency improvement of  $\text{Cs}_2\text{AgBiBr}_6$  PSC, X-ray photoelectron spectroscopy (XPS) was used to analyze the chemical state of hydrogenated  $\text{Cs}_2\text{AgBiBr}_6$  as shown in [Figs. 4a-4c](#) and [Supplementary Fig. 7](#). For the pristine  $\text{Cs}_2\text{AgBiBr}_6$  film, only one Cs 3d<sub>3/2</sub> XPS peak at 739.2 eV was present. However, after hydrogenating the  $\text{Cs}_2\text{AgBiBr}_6$  films for 600 s and 1,200 s, the Cs 3d<sub>3/2</sub> peak divided into two peaks: one shifts to a low binding energy of 738.7 eV (600 s) and then to 738.6 eV (1,200 s), the other one shifts to a high binding energy from 739.2 eV (0 s) to 740.6 eV (600 s) and then to 741.1 eV (1,200 s) ([Fig. 4a](#)). For Ag 3d<sub>3/2</sub> peak, the increase of hydrogenation time would induce an increase of binding energy from 374.0 eV to 374.1 eV and further to 374.2 eV ([Fig. 4b](#)). However, the major peak of Bi 4f<sub>5/2</sub> in  $\text{Cs}_2\text{AgBiBr}_6$  films keeps at around 164.7 eV ([Fig. 4c](#)), but a small peak appears at around 162.2 eV and 162.0 eV after 600 s and 1,200 s hydrogenation treatment. In addition, the binding energy position of Br 3d in  $\text{Cs}_2\text{AgBiBr}_6$  films almost unchanges after 600 s and 1,200 s hydrogenation treatment ([Supplementary Fig. 7](#)).

Although the hydrogenation process affects the chemical environment of Cs, Ag and Bi atoms in  $\text{Cs}_2\text{AgBiBr}_6$  lattice, the occupation position of  $\text{H}^*$  in the crystal lattice of  $\text{Cs}_2\text{AgBiBr}_6$  is still unknown. To settle this problem, DFT calculation with HSE+SOC band structures of host  $\text{Cs}_2\text{AgBiBr}_6$  is used to simulate the possible  $\text{H}^*$  positions in  $\text{Cs}_2\text{AgBiBr}_6$  lattice as shown in [Fig. 4d](#) and [Supplementary Fig. 8](#). There exists three different structure units in  $\text{Cs}_2\text{AgBiBr}_6$  lattice for  $\text{H}^*$  incorporation, including: Ag-Br-Cs hexahedron (named as  $\text{H}_1$ ), Bi-Br-Cs hexahedron ( $\text{H}_2$ ), and Cs-Br-Cs octahedron ( $\text{H}_3$ ) sites as shown in [Fig. 4d](#) and [Supplementary Fig. 9](#). Here the  $\text{H}^*$  may be a substitutional atom at the Br site in  $\text{H}_n(\text{Br})$  (where  $n=1, 2$ , or  $3$ ) ([Supplementary Figs. 9a-9c](#)) or as an interstitial hydrogen in  $\text{H}_n(\text{in})$  polyhedrons (insets in [Fig. 4d](#)). However, for the hydrogen substitution on Br site, the bandgap for all  $\text{H}_{1/2/3}(\text{Br})$  configurations almost unchanged as compared with the host  $\text{Cs}_2\text{AgBiBr}_6$  ([Supplementary Fig. 8](#) and [Supplementary Fig. 9a](#)). The inconsistency between theoretical simulation results and experimental results ([Fig. 1e](#)) indicates that the substitution of  $\text{H}^*$  at the Br sites is not the main contribution for the optimization of bandgap in hydrogenated  $\text{Cs}_2\text{AgBiBr}_6$ .

For the interstitial doping of  $\text{H}^*$  in  $\text{Cs}_2\text{AgBiBr}_6$  structure, there are three different positions, as shown in the  $\text{H}_1(\text{in})$ ,  $\text{H}_2(\text{in})$  and  $\text{H}_3(\text{in})$  structures in [Fig. 4d](#). Considering on the formation energies of  $\text{H}_1(\text{in})$ ,  $\text{H}_2(\text{in})$  and  $\text{H}_3(\text{in})$  structures, though  $\text{H}_3(\text{in})$  has the highest value, the difference between them are small, indicating the formation of  $\text{H}_1(\text{in})$ ,  $\text{H}_2(\text{in})$  and  $\text{H}_3(\text{in})$  in hydrogenated  $\text{Cs}_2\text{AgBiBr}_6$  are both possible ([Fig. 4d](#)). For the host  $\text{Cs}_2\text{AgBiBr}_6$ , its bandgap (by using the HSE+SOC model, [Supplementary Fig. 8](#)) has been determined to be indirect with a value of 1.98 eV, which is close

to the experimental one of 2.14 eV ([Fig. 1d](#)). However, for the three different types of  $H_n(\text{in})$  structures ([Fig. 4d](#)), interbands are formed between the upper valence band and lower conduction band, leading to the decreasing of effective bandgaps compared with the host  $\text{Cs}_2\text{AgBiBr}_6$  ([Supplementary Fig. 10](#)), which is consistent with the experimental result ([Fig. 2e](#)). And the physical model for the energy level positions of  $H_n(\text{in})$  structures are derived as shown in [Fig. 4e](#). On one hand, H-1s orbital couples with cation and forms the bonding state ([Supplementary Fig. 10](#)), which is higher than VBM ([Fig. 4e](#)); on the other hand, H-1s orbital couples with anion and forms antibonding state ([Supplementary Fig. 10](#)), which is higher than CBM ([Fig. 4e](#)). This physical model is well matched with the experimental energy-level diagram in hydrogenated  $\text{Cs}_2\text{AgBiBr}_6$  ([Fig. 2e](#) and [Fig. 2f](#)).

In addition, the variations of charges on Ag, Cs and Bi atom sites in different  $H_n(\text{in})$  structures are investigated by bader analysis and compared with the one in host structure, as shown in [Fig. 4f](#). The decreased bader charge of Ag atom in  $H_1(\text{in})$  means Ag losing some electrons to the surrounding atoms and leading to the increasing of Ag 3d binding energy. This is in agreement with the variation tendency of Ag 3d peak position shift in XPS results (increasing of binding energy in [Fig. 4b](#) and [Fig. 4g](#)), which indicates the existence of  $H_1(\text{in})$  in hydrogenated  $\text{Cs}_2\text{AgBiBr}_6$ . However, the increasing bader charge of Bi atom in  $H_2(\text{in})$  suggests a electron gain of Bi atom from the surrounding atoms ([Fig. 4f](#)), resulting in the decreasing binding energy of Bi [4f](#). This is consistent with the decrease of Bi 4f binding energy in XPS results ([Fig. 4c](#) and [Fig. 4g](#)) and reveals the formation of  $H_2(\text{in})$  in hydrogenated  $\text{Cs}_2\text{AgBiBr}_6$ . What's more, the existence of  $H_1(\text{in})$  and  $H_2(\text{in})$  structures would induce the decrease of bader charges ([Fig. 4f](#)) and increase of

binding energy of Cs atoms, which is well matched with the peak position increase of Cs 3d in XPS results ([Fig. 4a](#) and [Fig. 4g](#)). On the other hand, the presence of H<sub>3</sub>(in) induces an increase of bader charge of Cs atoms, which corresponds to a decreasing binding energy of Cs 3d ([Fig. 4a](#) and [Fig. 4g](#)). So, by analyzing the changes of bader charges and comparing them with XPS results ([Fig. 4](#)), we confirm that the interstitial doping of H\* in H<sub>1</sub>(in), H<sub>2</sub>(in) and H<sub>3</sub>(in) structures do exist in the hydrogenated Cs<sub>2</sub>AgBiBr<sub>6</sub>.

## Conclusion

In this paper, we have developed a novel hydrogenation method to modify the material properties of Cs<sub>2</sub>AgBiBr<sub>6</sub> film. After hydrogenating treatment of the Cs<sub>2</sub>AgBiBr<sub>6</sub> film from 0 s to 1,200 s, the light absorption at the wavelength ranged from 483 nm to 1,200 nm increases apparently, which corresponds to a decrease of bandgap from 2.14 eV to 1.61 eV. At the same time, the carrier concentration of the hydrogenated Cs<sub>2</sub>AgBiBr<sub>6</sub> films increases from  $1.42 \times 10^{12} \text{ cm}^{-3}$  to  $5.96 \times 10^{12} \text{ cm}^{-3}$ , and the carrier mobility and lifetime have also been largely improved from  $1.71 \text{ cm}^2 \text{V}^{-1} \text{s}^{-1}$  and 18.85 ns, to  $9.28 \text{ cm}^2 \text{V}^{-1} \text{s}^{-1}$  and 41.86 ns, respectively. Based on this, the hydrogenated Cs<sub>2</sub>AgBiBr<sub>6</sub> perovskite films were fabricated into solar cells, and the highest PCE of 6.27% is achieved, which is a record high efficiency of Cs<sub>2</sub>AgBiBr<sub>6</sub>-based perovskite solar cell. First-principle calculations confirm that hydrogen atoms are doped into the interstitial sites of Cs<sub>2</sub>AgBiBr<sub>6</sub> lattice, and the band couplings between hydrogen atoms and anion/cation alter the valence/conduction band levels, which agrees well with the experimental results. All these findings provide an effective lattice engineering strategy for preparing high-efficient and bandgap tunable lead-free inorganic perovskite solar cells, which are not only environment-friendly for

optoelectronic device applications, but also very stable in different working or storage environments. And this discovery may offer a good opportunity for exploring the next generation perovskite solar cell and other optoelectronic devices.

## Methods

### Materials

The experimental materials such as tin oxide ( $\text{SnO}_2$ , 15%), cesium bromide ( $\text{CsBr}$ , 99.9%), silver bromide ( $\text{AgBr}$ , 99.5%) and bismuth bromide ( $\text{BiBr}_3$ , 99%) were purchased from Alfa Aesar. Dimethylsulfoxide (DMSO, anhydrous 99.9% Sigma-Aldrich), isopropanol (IPA 99.5%, Aladdin), acetonitrile (99.8%, Sigma-Aldrich), 4-tertbutylpyridine (96%, Sigma-Aldrich), bis (trifluoromethane) sulfonimide lithium salt (99%, Xi'an Polymer Light Technology Corp), chlorobenzene (99%, Aladdin) and spiro-OMeTAD (99.5%, Xi'an Polymer Light Technology Corp) were used without further purification.

### Preparation of perovskite precursor solutions

In this work, we adopt a solution spin-coating method<sup>4</sup> to prepare high quality  $\text{Cs}_2\text{AgBiBr}_6$  films. Although the solubility of  $\text{Cs}_2\text{AgBiBr}_6$  in dimethylsulfoxide (DMSO) solution is only 0.6 mmol/mL, we still choose DMSO as the precursor solvent because of its relatively high value<sup>4</sup>. The  $\text{Cs}_2\text{AgBiBr}_6$  perovskite precursor solution (0.6 mmol/ml) was prepared by dissolving 212.81 mg  $\text{CsBr}$ , 187.77 mg  $\text{AgBr}$  and 448.68 mg  $\text{BiBr}_3$  into 1 mL of anhydrous solvent of DMSO. In order to ensure sufficient solubility and prepare high quality  $\text{Cs}_2\text{AgBiBr}_6$  perovskite film, the perovskite precursor solution was stirred at 70 °C in glove box for 12 h until the solutes were completely dissolved into the DMSO solvent and filtered through 0.45  $\mu\text{m}$  poly tetra fluoro

ethylene (PTFE) filtering membrane.

### Determination of the diffusion coefficient of atomic hydrogen in $\text{Cs}_2\text{AgBiBr}_6$ film

As shown in equation 2, the evolution of  $\frac{C}{C_s}$  values could be deduced as a change of hydrogenation time and atomic hydrogen diffusion coefficient ([Supplementary Fig. 5](#)). However, due to the thickness of  $\text{Cs}_2\text{AgBiBr}_6$  film is about 140 nm ([Supplementary Fig. 5f](#)), so the determination of  $\frac{C}{C_s}$  values at the top surface and bottom of a 140 nm thick  $\text{Cs}_2\text{AgBiBr}_6$  film is critical important as shown in [Supplementary Table 3](#). However, in practice, it is very difficult to quantify the atomic hydrogen concentration at the top surface and bottom of the hydrogenated  $\text{Cs}_2\text{AgBiBr}_6$  film, which inversely limits the analysis on the accurate diffusion coefficient of atomic hydrogen in  $\text{Cs}_2\text{AgBiBr}_6$  film. To settle this problem, we firstly extract the  $\frac{C'}{C'_{s'}}$  values from the experimental optical images in [Fig. 2a](#) and compare them with the simulated values  $\frac{C}{C_s}$  in [Supplementary Table 3](#). As shown above, the optical absorption properties of hydrogenated  $\text{Cs}_2\text{AgBiBr}_6$  film increases as the increasing of hydrogenation time (actually the hydrogen concentration increase), and film became much darker ([Fig. 2a](#)). From this point of view, it is assumed that the blackness values of the front and back side optical images (in [Fig. 2a](#)) are directly proportional to the average hydrogen concentration near the top and bottom surface of hydrogenated  $\text{Cs}_2\text{AgBiBr}_6$  film, respectively (as shown by  $C_s'$  and  $C'$  in [Supplementary Fig. 5g](#)). However, the hydrogen concentration is gradient distributed from the top surface to the bottom of film ([Fig. 2b](#)), this means that the experimental  $\frac{C'}{C'_{s'}}$  values must be larger than the simulated  $\frac{C}{C_s}$  values ( $\frac{C'}{C'_{s'}} > \frac{C}{C_s}$ ) ([Supplementary Fig. 5g](#)).

According to the experimental  $\frac{C'}{C'_{s'}}$  value of 0.205 at the hydrogenation time of 600 s ([Supplementary Table 3](#)), the simulated  $\frac{C}{C_s}$  value should be less than 0.205 and we can find that

only a diffusion coefficient smaller than  $1 \times 10^{-13}$  cm<sup>2</sup>/s ( $\frac{C}{C_s} = 0.203$ ) is appropriate. Meanwhile, such a diffusion efficient of  $1 \times 10^{-13}$  cm<sup>2</sup>/s is applicable to the  $\frac{C}{C_s'}$  and  $\frac{C}{C_s}$  values at the hydrogenation time of 1,200 s ( $\frac{C}{C_s'} = 0.405 > \frac{C}{C_s} = 0.366$ ), 1,800 s ( $\frac{C}{C_s'} = 0.834 > \frac{C}{C_s} = 0.460$ ), 2,400 s ( $\frac{C}{C_s'} = 0.963 > \frac{C}{C_s} = 0.522$ ) and 3,000 s ( $\frac{C}{C_s'} \approx 1.000 > \frac{C}{C_s} = 0.571$ ). It should point out that, as the hydrogenation time increasing up to 3,000 s, the front and back sides color of the hydrogenated Cs<sub>2</sub>AgBiBr<sub>6</sub> film are both black, which takes a  $\frac{C}{C_s'} \approx 1.000$ . It indicates that a large number of hydrogen atoms must have reached to the bottom of the Cs<sub>2</sub>AgBiBr<sub>6</sub> film after 3,000 s hydrogenation treatment. However, from the data in [Supplementary Table 3](#), if the diffusion efficient is less than  $1 \times 10^{-14}$  cm<sup>2</sup>/s, then the  $\frac{C}{C_s}$  value equals to 0.074 even after a 3,000 s of hydrogen diffusion. From all the analyses above, we can conclude that the diffusion coefficient  $D$  of atomic hydrogen in Cs<sub>2</sub>AgBiBr<sub>6</sub> film must be located in the range between  $1 \times 10^{-14}$  cm<sup>2</sup>/s to  $1 \times 10^{-13}$  cm<sup>2</sup>/s.

## Device fabrication

Inorganic lead-free double PSCs with typical planar structure ITO/SnO<sub>2</sub>/perovskite/spiro-OMeTAD/Au were fabricated as follows: The indium tin oxide (ITO) glass substrates were washed by ultrasonic cleaning in acetone, ethanol, detergent and deionized water for 30 min, respectively. After drying, the ITO glass substrates were treated by an oxygen plasma for 10 min to improve the hydrophilicity of the substrate surface. The original solution of SnO<sub>2</sub> was mixed with deionized water in the volume ratio of 1:5. SnO<sub>2</sub> solution of 50 μL was dynamically spin-coated on the clean ITO glass substrates at 3,000 rpm for 30 s. Then the SnO<sub>2</sub> electron transport layer film was annealed at 150 °C for 30 min in air. In order to improve the surface coverage and film quality, a lot of efforts were made in our research such as: increasing

the spin-coating temperature<sup>43</sup> to 40 °C and using isopropanol (IPA) solution as anti-solvent during the spin-coating process as shown in Fig. 1a. Cs<sub>2</sub>AgBiBr<sub>6</sub> perovskite films were deposited in the glove box full of N<sub>2</sub> using traditional solvent-quenching method with IPA as the antisolvent. 50 μL Cs<sub>2</sub>AgBiBr<sub>6</sub> precursor solution was dynamically spin-coated at 40 °C on the cleaned ITO glass substrates at 5,000 rpm for 50 s, and 300 μL antisolvent (IPA solvent) was spin-coated at 10 s, which was just before the atomization point. Then the film was annealed at 290 °C for 5 min. In order to doping the hydrogen atoms into Cs<sub>2</sub>AgBiBr<sub>6</sub> film, the film was hydrogenated through a plasma treatment (Soft Plasma Cleaner SPC 150) with the source power of 30 W in Ar and H<sub>2</sub> mix (80 wt.% H<sub>2</sub>) gas. Spiro-OMeTAD was used as the hole transport layer. To prepare the Spiro-OMeTAD solution, 45 μL Li-TFSI solution (170 mg/mL acetonitrile), 10 μL 4-TBP and 90 mg Spiro-OMeTAD were mixed into 1 mL chlorobenzene solvent and then stirred in a dark environment in N<sub>2</sub> glove box until fully dissolved. After that, 50 μL Spiro-OMeTAD solution was dynamically spin-coated on the surface of the perovskite film at 3,000 rpm for 30 s in N<sub>2</sub> glove box. After the spin-coating, it was placed in oxygen atmosphere and kept away from light for 24 hours to make Spiro-OMeTAD layer fully oxidized. Gold (Au) electrode was coated on the Spiro-OMeTAD hole transport layer by thermal evaporation. The interface between the electrode film and the hole transport layer was well combined. The electrode film was uniform with the thickness of about 60 nm.

### Characterization of solar cells and films

We measured *J-V* curves of PSC devices in air with Keithley 2400 Source under AM 1.5 (100 mW cm<sup>-2</sup>, xenon lamp, Newport) irradiance level. All the I-V measurements were carried out in ambient air environment. The area of each device is 0.2 cm<sup>2</sup>. During measuring, a 0.04 cm<sup>2</sup>

non-reflective mask was used to define the accurate active cell area with the testing range of reverse scanning voltage from 1.2 V to -0.2 V (step 0.02V). The optical absorption spectrum was measured in air by an ultraviolet-visible near-infrared spectrophotometer (UV-Vis) (Hitachi, UH-4150), and the spectral wavelength range in our results was from 300 nm to 1,200 nm. The XRD spectra of the perovskite films were obtained with Bruker D8 Advance X-ray diffractometer using Cu K<sub>α</sub> radiation ( $\lambda=1.5418 \text{ \AA}$ ). Scanning electron microscope (Helios Nanolab 600i) operated at 5 kV was used to characterize the microstructure of films and cross-section of perovskite solar cell. The carrier lifetime was obtained by using B411 (FLS-1000). The XPS and UPS spectrums were measured through XPS system (ESCALAB 250Xi). The electrical properties were measured with four-point probe method by using Hall-effect measurement system (Eastchanging ET 9000).

### **The preparation and characterization of TEM samples**

The TEM sample of Cs<sub>2</sub>AgBiBr<sub>6</sub> perovskite devices were prepared through Focused Ion Beam (FIB) system (Helios Nanolab 600i) operating at 2 kV-30 kV. In order to make sure the cleanliness of the device surface, the sample was first cleaned by N<sub>2</sub> gas gun before putting into the FIB system. Firstly, we selected one flat area and deposited 1.2  $\mu\text{m}$  thick Pt layer (200 nm e-beam deposition with 5 kV, 2.7 nA followed by 1  $\mu\text{m}$  ion beam deposition with 30 kV, 30 pA) onto the surface of device, which could protect the sample from the harm of Ga ion beam damage. Then, the specimen was crosscut and thinned to about 200 nm from 1.5  $\mu\text{m}$  by using 30 kV Ga ion beam. Lastly, in order to remove the surface damage layer, a final polishing was performed first using 5 kV, 15 pA and further using 2 kV, 23 pA Ga ion beam. TEM sample of Cs<sub>2</sub>AgBiBr<sub>6</sub> films was prepared by transfer of as-grown Cs<sub>2</sub>AgBiBr<sub>6</sub> films onto a TEM grid. Samples were investigated

by using probe spherical aberration corrected transmission electron microscope (FEI Titan G2) with 300 kV accelerating voltage and gain the images using STEM-HAADF detectors. The microscopic chemical compositions of the samples were analyzed by using high efficient “Super X” Engery Disperse Spectroscopy (EDS) detector. The energy resolution of the super-EDX is 137 eV. The EDS data were collected and processed by using Esprit 1.9 software.

### DFT calculation

First-principles calculations were performed using density functional theory (DFT) as implemented in the VASP code.<sup>44,45</sup> The electron and core interactions were included using the frozen-core projected augmented wave approach.<sup>46</sup> The generalized gradient approximation of Perdew–Burke–Ernzerhof (PBE)<sup>47</sup> was used for the exchange correlation functional. The kinetic energy cutoff for plane-wave basis functions is set to 400 eV. K-point meshes with grid spacings of  $2\pi \times 0.025 \text{ \AA}^{-1}$  or smaller were used for Brillouin zone integration. The structures of  $\text{Cs}_2\text{AgBiBr}_6$  with the  $\text{Fm}\bar{3}m$  space group were relaxed until the total energies converged to  $10^{-4}$  eV. All the atoms are fully relaxed for the substitutional hydrogen ( $\text{H}_{1/2/3}(\text{Br})$ ) and interstitial hydrogens ( $\text{H}_{1/2/3}(\text{in})$ ) in  $\text{Cs}_2\text{AgBiBr}_6$  lattice. The formation energies and Bader charges of  $\text{H}_{1/2/3}(\text{in})$  are conducted using PBE functional. The formation energy are defined as:  $\Delta E_f = E(H_i) - E(\text{host}) - 0.5 \cdot E(\text{H}_2)$ , where  $E(H_i)$ ,  $E(\text{host})$  and  $E(\text{H}_2)$  are the total energies of  $H_i$ , pure  $\text{Cs}_2\text{AgBiBr}_6$  and hydrogen molecule, respectively. Whereas, a hybrid Heyd–Scuseria–Ernzerhot (HSE)<sup>48</sup> with a standard 25% Hartree Fock exchange was used for evaluating the bandgaps. Due to the heavy element Bi in  $\text{Cs}_2\text{AgBiBr}_6$ , spin-orbit coupling (SOC) effect was also taken into consideration in the calculations.

### Ageing process of perovskite films

$\text{Cs}_2\text{AgBiBr}_6$  perovskite films could change from yellow to black after hydrogenation process, indicating the large increase in light absorption. Then we ageing the hydrogenated  $\text{Cs}_2\text{AgBiBr}_6$  films at different condition including: 25 °C/ $\text{N}_2$ /dark, 25 °C/ $\text{N}_2$ /1-sun-light-illumination and 85 °C/ $\text{N}_2$ /dark environments. Then we take optical images of the hydrogenated  $\text{Cs}_2\text{AgBiBr}_6$  films at different ageing time and gain the bandgap values of the films through UV-Vis.

## Reference

- 1 NREL. *Best Research-Cell Efficiency chart* <https://www.nrel.gov/pv/cell-efficiency.html> (accessed 17 March 2021).
- 2 Jeon, N. J. et al. Compositional engineering of perovskite materials for high-performance solar cells. *Nature*. **517**, 476-480 (2015).
- 3 Bi, D. et al. Efficient luminescent solar cells based on tailored mixed-cation perovskites. *Sci. Adv.* **2**, e1501170 (2016).
- 4 Yang, W. S. et al. Iodide management in formamidinium-lead-halide-based perovskite layers for efficient solar cells. *Science*. **356**, 1376-1379 (2017).
- 5 Correa-Baena, J. P. et al. Promises and challenges of perovskite solar cells. *Science*. **358**, 739-744 (2017).
- 6 Babayigit, A., Ethirajan, A., Muller, M. & Conings, B. Toxicity of organometal halide perovskite solar cells. *Nat. Mater.* **15**, 247-251 (2016).
- 7 Leijtens, T. et al. Stability of metal halide perovskite solar cells. *Adv. Energy Mater.* **5**, 1500963 (2015).
- 8 Berhe, T. A. et al. Organometal halide perovskite solar cells: degradation and stability.

- Energy Environ. Sci.* **9**, 323-356 (2016).
- 9 Shi, Z. et al. Lead-Free organic-inorganic hybrid perovskites for photovoltaic applications:  
recent advances and perspectives. *Adv. Mater.* **29**, 1605005 (2017).
- 10 Hayase, S. Research following Pb perovskite solar cells. *Electrochemistry*. **85**, 222-225  
(2017).
- 11 Zhang, C., Gao, L., Hayase, S. & Ma, T. Current advancements in material research and  
techniques focusing on lead-free perovskite solar cells. *Chem. Lett.* **46**, 1276-1284 (2017).
- 12 Zuo, C. et al. Advances in perovskite solar cells. *Adv. Sci.* **3**, 1500324 (2016).
- 13 Ran, C. et al. Bilateral interface engineering toward efficient 2D–3D bulk heterojunction  
tin halide lead-free perovskite solar cells. *ACS Energy Lett.* **3**, 713-721, (2018).
- 14 Zhang, Y.-Y. et al. Intrinsic instability of the hybrid halide perovskite semiconductor  
 $\text{CH}_3\text{NH}_3\text{PbI}_3$ . *Chin. Phys. Lett.* **35**, 036104 (2018).
- 15 Chung, I. et al.  $\text{CsSnI}_3$ : Semiconductor or metal? High electrical conductivity and strong  
near-infrared photoluminescence from a single material. High hole mobility and  
phase-transitions. *J. Am. Chem. Soc.* **134**, 8579-8587 (2012).
- 16 Chen, J. et al. Tin (IV)-tolerant vapor phase growth and photophysical properties of  
aligned cesium tin halide perovskite ( $\text{CsSnX}_3$ , X=Br, I) nanowires. *ACS. Energy. Lett.* **4**,  
1045-1052 (2019).
- 17 Savory, C. N., Walsh, A. & Scanlon, D. O. Can Pb-free halide double perovskites support  
high-efficiency solar cells? *ACS. Energy. Lett.* **1**, 949-955 (2016).
- 18 Greul, E., Petrus, M. L., Binek, A., Docampo, P. & Bein, T. Highly stable, phase pure  
 $\text{Cs}_2\text{AgBiBr}_6$  double perovskite thin films for optoelectronic applications. *J. Mater. Chem.*

- A. **5**, 19972-19981 (2017).
- 19 Slavney, A. H., Hu, T., Lindenberg, A. M. & Karunadasa, H. I. A bismuth-halide double perovskite with long carrier recombination lifetime for photovoltaic applications. *J. Am. Chem. Soc.* **138**, 2138-2141 (2016).
- 20 McClure, E. T., Ball, M. R., Windl, W. & Woodward, P. M.  $\text{Cs}_2\text{AgBiX}_6$  (X = Br, Cl): new visible light absorbing, lead-free halide perovskite semiconductors. *Chem. Mater.* **28**, 1348-1354 (2016).
- 21 Pan, W. et al.  $\text{Cs}_2\text{AgBiBr}_6$  single-crystal X-ray detectors with a low detection limit. *Nat. Photonics.* **11**, 726-732 (2017).
- 22 Bartesaghi, D. et al. Charge carrier dynamics in  $\text{Cs}_2\text{AgBiBr}_6$  double perovskite. *J. Phys. Chem. C.* **122**, 4809-4816 (2018).
- 23 Milot, R. L., Eperon, G. E., Snaith, H. J., Johnston, M. B. & Herz, L. M. Temperature-dependent charge-carrier dynamics in  $\text{CH}_3\text{NH}_3\text{PbI}_3$  perovskite thin films. *Adv. Funct. Mater.* **25**, 6218-6227 (2015).
- 24 Ning, W. et al. Long electron-hole diffusion length in high-quality lead-free double perovskite films. *Adv. Mater.* **30**, 1706246 (2018).
- 25 Fan, P. et al. Single-source vapor-deposited  $\text{Cs}_2\text{AgBiBr}_6$  thin films for lead-free perovskite solar cells. *Nanomaterials.* **9**, 1760 (2019).
- 26 Wang, M. et al. High-quality sequential-vapor-deposited  $\text{Cs}_2\text{AgBiBr}_6$  thin films for lead-free perovskite solar cells. *Sol. RRL.* **2**, 1800217 (2018).
- 27 Kung, P.-K. et al. Lead-free double perovskites for perovskite solar cells. *Sol. RRL.* **4**, 1900306 (2019).

- 28 Gao, W. et al. High-quality  $\text{Cs}_2\text{AgBiBr}_6$  double perovskite film for lead-free inverted planar heterojunction solar cells with 2.2% efficiency. *Chemphyschem.* **19**, 1696-1700 (2018).
- 29 Li, Q. et al. High-pressure band-gap engineering in lead-free  $\text{Cs}_2\text{AgBiBr}_6$  double perovskite. *Angew. Chem. Int. Ed.* **56**, 15969-15973 (2017).
- 30 Ji, F. et al. Lead-free halide double perovskite  $\text{Cs}_2\text{AgBiBr}_6$  with decreased band gap. *Angew. Chem. Int. Ed.* **59**, 1-5 (2020).
- 31 Yang, J., Zhang, P. & Wei, S.-H. Band structure engineering of  $\text{Cs}_2\text{AgBiBr}_6$  perovskite through order-disordered transition: a first-principle study. *J. Phys. Chem. Lett.* **9**, 31-35 (2018).
- 32 Davis, E. A. & Mott, N. F. Conduction in non-crystalline systems v. conductivity, optical absorption and photoconductivity in amorphous semiconductors. *Philos. Mag.* **22**, 0903-0922 (1970).
- 33 Viezbicke, B. D., Patel, S., Davis, B. E. & Birnie, D. P. Evaluation of the tauc method for optical absorption edge determination:  $\text{ZnO}$  thin films as a model system. *Phys. Status. Solidi. B.* **252**, 1700-1710 (2015).
- 34 Mehrer, Helmut. Diffusion in Solids (Berlin Heidelberg, Springer-Verlag Berlin Heidelberg, 2007), **P42**.
- 35 Olden, V., Alvaro, A., & Akselsen, O. M. Hydrogen diffusion and hydrogen influenced critical stress intensity in an API X70 pipeline steel welded joint - experiments and FE simulations. *Int. J. Hydrogen. Energy.* **37(15)**, 11474-11486 (2012).
- 36 Martins, T. R. D. B., Azambuja, V. M., Santos, D. S. D., & Tavares, S. S. M. Influence of

- nanoxides on diffusivity and solubility of hydrogen in Pd-based alloys. *Mater. Res.* **20**, 111-116 (2017).
- 37 Lee, J., Park, C., Park, H., & Kang, N. Effective hydrogen diffusion coefficient for CoCrFeMnNi high-entropy alloy and microstructural behaviors after hydrogen permeation. *Int. J. Hydrogen. Energy.* **45(16)**, 10227-10232 (2020).
- 38 Kürten, D., Khader, I., & Kailer, A. Determining the effective hydrogen diffusion coefficient in 100Cr6. *Mater. Corros.* **71(6)**, 918-923 (2020).
- 39 Zheng, G., Popov, B. N., & White, R. E. Electrochemical determination of the diffusion coefficient of hydrogen through an LaNi<sub>4.25</sub>Al<sub>0.75</sub> electrode in alkaline aqueous solution. *J. Electrochem. Soc.* **142(8)**, 2695 (1995).
- 40 Sheikholeslam, S. A. et al. Hydrogen diffusion characterization of amorphous yttrium stabilized zirconia dielectrics. *2016 IEEE 16th International Conference on Nanotechnology (IEEE-NANO)*. IEEE (2016).
- 41 Yu, G. C. A comparison between proton and hydrogen chemical diffusion coefficients of titanium oxide films. *Phys. Stat. sol (a)*. **198(2)**, 302-311 (2003).
- 42 Weidinger, A. et al. Hydrogen diffusion in chalcopyrite solar cell materials. *MRS Online Proceedings Library Archive*. **513** (1998).
- 43 Nie, W. et al. High-efficiency solution-processed perovskite solar cells with millimeter-scale grains. *Science*. **347**, 522-525 (2015).
- 44 Kresse, G. & Furthmüller, J. Efficient iterative schemes for Ab initio total-energy calculations using a plane-wave basis set. *Phys. Rev. B*. **54**, 11169-11186 (1996).
- 45 Kresse, G. & Furthmüller, J. Efficiency of ab-initio total energy calculations for metals

- and semiconductors using a plane-wave basis set. *Comput. Mater. Sci.* **6**, 15-50 (1996).
- 46 Kresse, G. & Joubert, D. From ultrasoft pseudopotentials to the projector augmented-wave method. *Phys. Rev. B.* **59**, 1758-1775 (1999).
- 47 Perdew, J. P., Burke, K., & Ernzerhof, M. Generalized gradient approximation made simple. *Phys. Rev. Lett.* **77**, 3865-3868 (1996).
- 48 Heyd, J. & Scuseria, G. E. Hybrid functionals based on a screened coulomb potential. *J. Chem. Phys.* **118**, 8207 (2003).

### Acknowledgements

This work was supported by the Beijing Innovation Team Building Program, China (IDHT20190503), the National Natural Science Foundation of China (11704015, 51621003, 12074016), the General Program of Science and Technology Development Project of Beijing Municipal Education Commission (KM202110005003), and the National Key Research and Development Program of China (2016YFB0700700).

### Author contributions

Yue Lu and Manling Sui conceived and designed the experiments. Zeyu Zhang prepared the samples, performed the measurement of X-ray Diffraction, Scanning electron microscopy, Ultraviolet-visible absorption, hall effect, Time-resolved photoluminescence, ultraviolet photoelectron spectroscopy, X-ray photoelectron spectroscopy, Transmission electron microscope, Current density-voltage curve and calculation the diffusion coefficient. Qingde Sun, Su-Huai Wei and Feng Lu did the theoretical calculations. Xulin Mu prepared the provskite film. Zeyu Zhang, Yue Lu, Manling Sui and Su-Huai Wei analyzed the data and co-wrote the paper. All authors discussed the results and revised the manuscript.

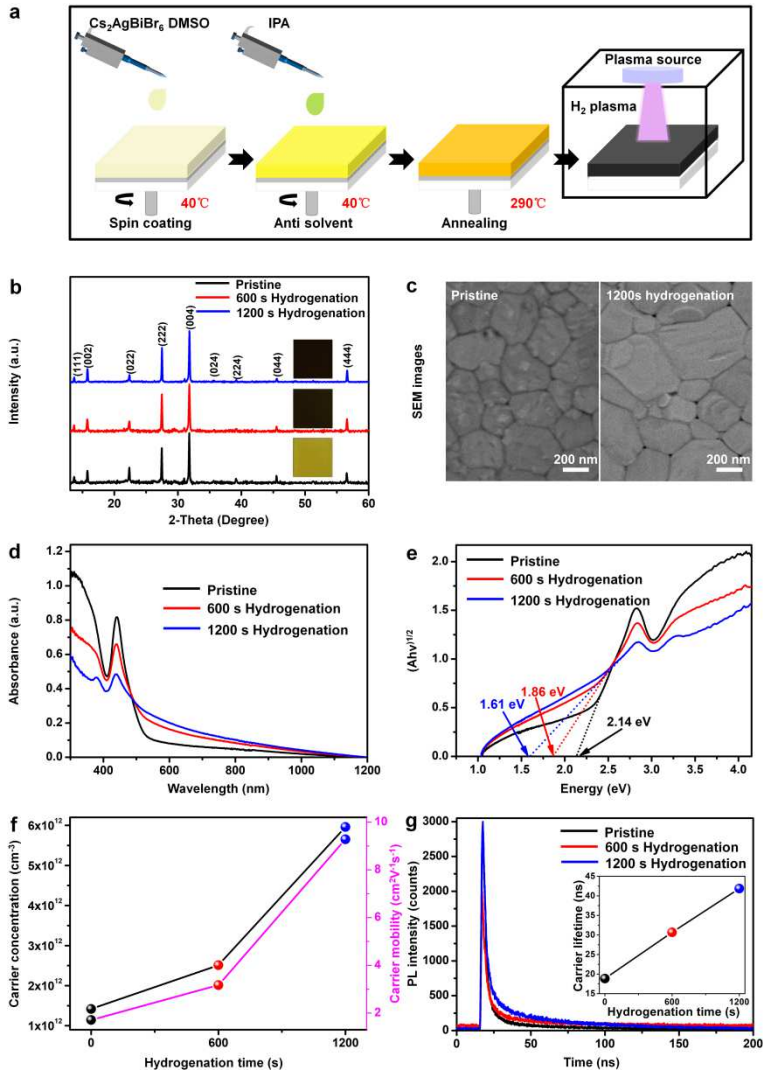


**Figure 1. Fabrication of the hydrogenated  $\text{Cs}_2\text{AgBiBr}_6$  perovskite films and the photoelectrical property characterization.** **a** The preparation method of  $\text{Cs}_2\text{AgBiBr}_6$  perovskite films during the hydrogenation treatment in hydrogen gas plasma. **b** X-ray Diffraction (XRD) patterns of the  $\text{Cs}_2\text{AgBiBr}_6$  perovskite films with different hydrogenation time (inserts show the optical pictures of the corresponding  $\text{Cs}_2\text{AgBiBr}_6$  films). **c** Scanning electron microscopy (SEM) images of the pristine  $\text{Cs}_2\text{AgBiBr}_6$  film and the 1,200 s hydrogenated  $\text{Cs}_2\text{AgBiBr}_6$  film. **d** Ultraviolet-visible absorption spectra (UV-vis) of the  $\text{Cs}_2\text{AgBiBr}_6$  perovskite films with different hydrogenation time. **e** Tauc plots of the  $\text{Cs}_2\text{AgBiBr}_6$  perovskite films with different hydrogenation time. **f** Carrier mobility and carrier concentration of the  $\text{Cs}_2\text{AgBiBr}_6$  perovskite films with time. **g** PL intensity and carrier lifetime.

different hydrogenation time. **g** Time-resolved photoluminescence (TRPL) and the measurement of carrier lifetime (inset) of  $\text{Cs}_2\text{AgBiBr}_6$  perovskite films with different hydrogenation time.

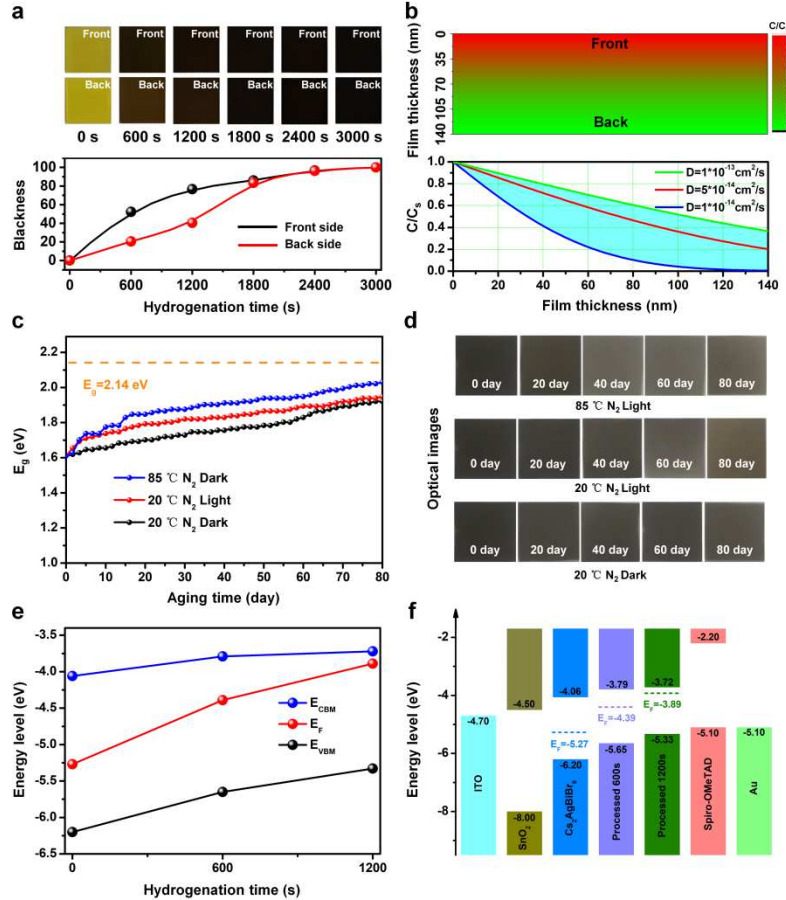


**Figure 2. The distribution of atomic hydrogen, environmental stability and energy level in the hydrogenated  $\text{Cs}_2\text{AgBiBr}_6$  film.** **a** The optical images of the  $\text{Cs}_2\text{AgBiBr}_6$  films with different hydrogenation time (top) and the blackness evolution of their corresponding images at the front and back sides (bottom). **b** The schematic diagram of the simulated distribution of atomic hydrogen in hydrogenated  $\text{Cs}_2\text{AgBiBr}_6$  film according to a diffusion coefficient of  $5 \times 10^{-14} \text{ cm}^2/\text{s}$  (top), and the diffusion curve of  $\text{H}^*$  based on different diffusion coefficient at the depth direction of film (bottom). **c** Evolution of the bandgap values of hydrogenated  $\text{Cs}_2\text{AgBiBr}_6$  films as storing in  $\text{N}_2$ , 1 sun light illumination and  $85^\circ\text{C}$  heating environments. **d** The photo-images (Front side) in  $\text{N}_2$ , 1 sun light illumination and  $85^\circ\text{C}$  heating environments. **e** The energy level evolution of  $E_{\text{CBM}}$ ,  $E_F$ , and  $E_{\text{VBM}}$  with hydrogenation time. **f** The energy band diagram of the device structure.

for stability of the hydrogenated  $\text{Cs}_2\text{AgBiBr}_6$  films at  $\text{N}_2$ , light illumination and  $85^\circ\text{C}$  heating environments, respectively. **e** The energy level of  $E_{CBM}$ ,  $E_{VBM}$  and  $E_F$  (femi level) in  $\text{Cs}_2\text{AgBiBr}_6$  films with different hydrogenation time (0 s, 600 s and 1,200 s). **f** Energy-level diagram of the functional layers in hydrogenated  $\text{Cs}_2\text{AgBiBr}_6$  perovskite solar cell.

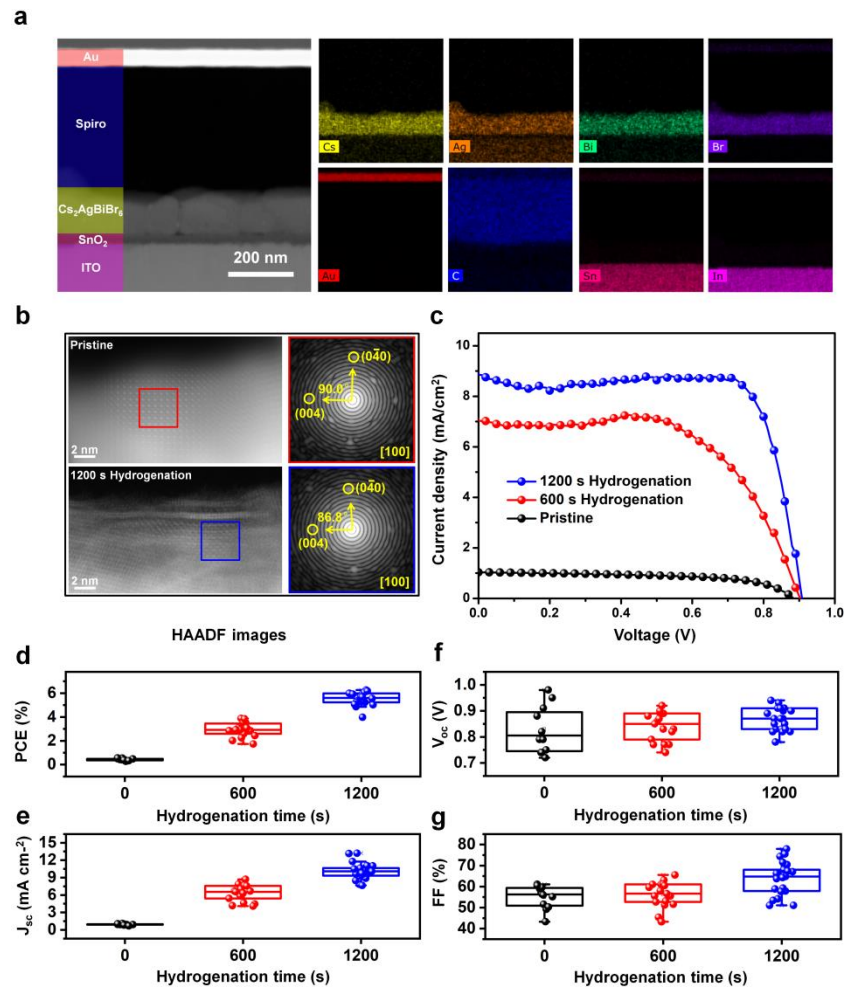


**Figure 3. Fabrication of hydrogenated  $\text{Cs}_2\text{AgBiBr}_6$  perovskite solar cell and the corresponding photoelectrical performance.** **a** High-angle annular dark field (HAADF) image and corresponding EDS mapping of the cross-section sample of the hydrogenated  $\text{Cs}_2\text{AgBiBr}_6$  perovskite solar cell. **b** HAADF images of pristine and hydrogenated  $\text{Cs}_2\text{AgBiBr}_6$  films, and the corresponding Fast Fourier transform (FFT) images for the areas marked by red and blue boxes. **c**

Current density-voltage ( $J-V$ ) curve of the champion  $\text{Cs}_2\text{AgBiBr}_6$  PSCs with different hydrogenation time (0 s, 600 s and 1,200 s). **d** The average photoelectric conversion efficiency (PCE) distribution of  $\text{Cs}_2\text{AgBiBr}_6$  PSCs with different hydrogenation time (0 s, 600 s and 1,200 s). **e** The average short-circuit current density ( $J_{sc}$ ) distribution of  $\text{Cs}_2\text{AgBiBr}_6$  PSCs with different hydrogenation time (0 s, 600 s and 1,200 s). **f** The average open-circuit voltage ( $V_{oc}$ ) distribution of  $\text{Cs}_2\text{AgBiBr}_6$  PSCs with different hydrogenation time (0 s, 600 s and 1,200 s). **g** The average fill factor ( $FF$ ) of  $\text{Cs}_2\text{AgBiBr}_6$  PSCs with different hydrogenation time (0 s, 600 s and 1,200 s).

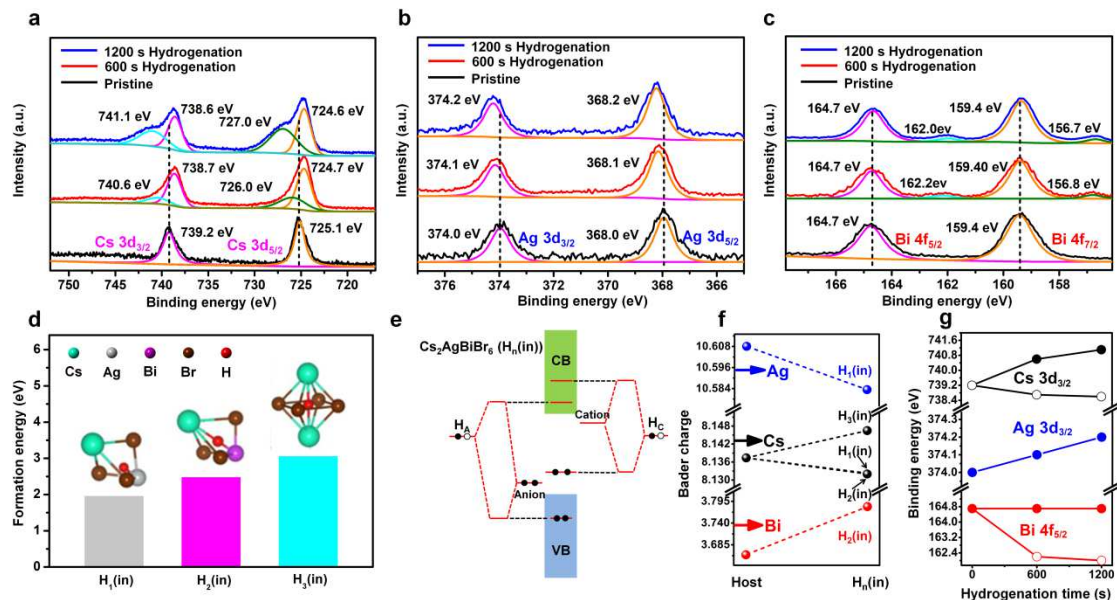


**Figure 4.** **a-c** X-ray photoelectron spectroscopy (XPS) spectra of Cs 3d, Ag 3d and Bi 4f in  $\text{Cs}_2\text{AgBiBr}_6$  films with different hydrogenation time (0 s, 600 s and 1,200 s). **d** The formation energies of  $\text{H}_1(\text{in})$ ,  $\text{H}_2(\text{in})$  and  $\text{H}_3(\text{in})$ . Here,  $\text{H}_n(\text{in})$ , where  $n=1, 2$ , or 3, presents the H atom in the interstitial position of the  $\text{H}_n$  polyhedrons surrounded by Cs-Br-Ag ( $\text{H}_1$ ), Cs-Br-Bi ( $\text{H}_2$ ), and Cs-Br-Cs ( $\text{H}_3$ ), respectively. Cs, Ag, Bi, Br and H atoms are represented by cyan, light grey, purple, brown and red dots, respectively. **e** Schematic band coupling models of  $\text{H}_n(\text{in})$  showing energy level positions when the H 1s orbital is coupled to anion (forming donor) and cation (forming acceptor) levels ( $\text{H}_A$  (coupled from interstitial  $\text{H}_n(\text{in})$  and anion) and  $\text{H}_C$  (coupled from interstitial  $\text{H}_n(\text{in})$  and cation)). **f** Bader charge variations of Ag, Bi, and Cs atoms in the host and next to the interstitial  $\text{H}^*$  in the  $\text{H}_n(\text{in})$  polyhedrons. **g** The variation tendency of binding energy of Cs 3d<sub>3/2</sub>, Ag 3d<sub>3/2</sub> and Bi 4f<sub>5/2</sub> peaks as the increase of hydrogenation time.

## Supplementary Files

This is a list of supplementary files associated with this preprint. Click to download.

- [Supplementaryinformation.docx](#)